# REVIEW ON FIBER MORPHOLOGY OBTAINED BY BUBBLE ELECTROSPINNING AND BLOWN BUBBLE SPINNING

by

***Ji-Huan HE*[a,b*], *Hai-Yan KONG*[a], *Rui-Rui YANG*[b], *Hao DOU*[a], *Naeem FARAZ*[b], *Liang WANG*[b], and *Chao FENG*[b]**

[a] National Engineering Laboratory for Modern Silk,
College of Textile and Clothing Engineering,
Soochow University, Suzhou, China
[b] Research Institute of Donghua University, Shanghai, China

Review paper
DOI: 10.2298/TSCI1205263H

*Here we show an intriguing phenomenon in the bubble electrospinning process that the ruptured film might be stripped upwards by an electronic force to form a very thin and long plate-like strip, which might been received in the metal receiver as discontinuous backbone-like wrinkled materials, rather than smooth nanofibers or microspheres. The processes are called the bubble electrospinning. The electronic force can be replaced by a blowing air, and the process is called as the blown bubble spinning. We demonstrate that the size and thickness of the ruptured film are the crucial parameters that are necessary to understand the various observations including beads and nanoporous materials. We identify the conditions required for a ruptured film to form discontinuous structure, and a critical width of the ruptured film to form a cylindrical fiber, above which a long and thin plate-like strip might be obtained, and a criterion for oscillatory jet diameter, which leads to bead morphology of the obtained fibers. The space of the adjacent beads depends on the fiber size. We anticipate our assay to be a starting point for more sophisticated study of the bubble electrospinning and the blown bubble spinning and for mass-production of both nanofibers and nanoscale discontinuous materials.*

Key words: *bubble electrospinning, blown bubble spinning, nanoscale discontinuous material, nanoporous materials, non-linear differential equation, nanofibers, beads, instability, Chauchy's inequality, non-linear oscillator*

## Introduction

Thin liquid films, such as soap bubbles, have been found wide applications in medicine [1], chemistry [2], food engineering [3], and nanotechnology [4] as well, but little was known that a polymer bubble can be used for nanofiber fabrication. When a polymer bubble under an electrostatic field ruptures, the surface tension leads to surface minimization of some film fragments, and daughter bubbles are formed [5, 6], while the electrostatic force ejects some fragments upwards, the process is called as the bubble electrospinning [7-11].

* Corresponding author; e-mail: hejihuan@suda.edu.cn

We can also use a blowing air instead of the electrostatic force to pull a polymer bubble up to finish a similar spinning process as the bubble electrospinning, and the process is called as the blown bubble spinning. Attempts to understand the processes have mostly focused on fabrication of smooth nanofibers. However, the precise mechanism of the nanofiber production using polymer bubbles is rare and preliminary, though soap bubbles have been studied extensively for over a century starting from the pioneering research by Schwarz in 1884 for the theory of minimal surface [12]. Now micro/nano bubbles become hot topics in heat transfer [13], MEMS applications [14], carrier of anti-cancer drugs [15], optical microbubble resonator [16], and ultrasound-targeted microbubble destruction [17]. The most interesting property of a bubble is that the surface tension of a bubble depends geometrically upon its size. According to the Young-Laplace equation [18, 19], the surface tension of a spherical bubble can be expressed as:

$$\sigma = \frac{1}{4} r \Delta p \tag{1}$$

where $\sigma$ is the surface tension, $r$ – the radius of the bubble, $\Delta p$ – the pressure difference; this formulation is still valid for nanobubble surface tension [20, 21].

In this paper, we summarize fiber morphology obtained from a polymer bubble.

## Experimental details

The experiment set-up is illustrated in fig. 1. When a high voltage is added, it induces charges into the bubble surface, these quickly relax to the bubble surface. The coupling of surface charge and the external electric field creates a tangential stress, resulting in the deformation of the bubble, which moves slowly upwards, and the thickness of the bubble wall becomes thinner and thinner. Tarkan *et al*. found that the initial thickness of a solvent-coated air bubble is about 3 μm, and the rupture thickness is less than 500 nm [22]. Similarly for a charged polymer bubble under the electrostatic field, the thinning wall cannot afford the electronic force. Once the electric field exceeds the critical value needed to overcome the surface tension, a hole is created somewhere in the film and the bubble is exploded suddenly.

Polylactide (PLA) particles with two different molecular weights of $M_\eta \approx 80000$ and $M_\eta \approx 100000$ were bought from Shenzhen Bright China Industrial Co. Ltd. (injection-moulding grade). N, N-dimethylfomamide (DMF, boiling point: 152.8 °C, vapor pressure: 3.47 mbar at 20 °C) and Dichloromethane (DCM, boiling point: 40 °C, vapor pressure: 475 mbar at 20 °C) were purchased from Shanghai Chemical Reagent Co. Ltd. All stuffs were used as received without further purification.

Three different spinning solutions were used. A 10 wt.% PLA solution ($M_\eta \approx 80000$) and a 15 wt.% PLA ($M_\eta \approx 100000$) solution were prepared by dissolving PLA particles into DMF solvent, and the concentration of the third PLA ($M_\eta \approx 100000$) solution with DCM as solvent was 8 wt.%. The applied voltage was 15 kV and the distance between the solution surface and the metal receiver was kept at 15 cm. All the experiments were carried on at temperature 20 °C with the relative humidity of 45%.

The morphology of the bubble-electrospun nanofibers was observed by Field Emission-Scanning Electronic Microscopy (S-4800, Hitachi Ltd., Japan), and the process of bubble-electrospinning was filmed by Motion Analyzing Microscope (VW-5000E, Keyence Ltd., Japan). We used Image J software to measure the diameter of nanofibers.

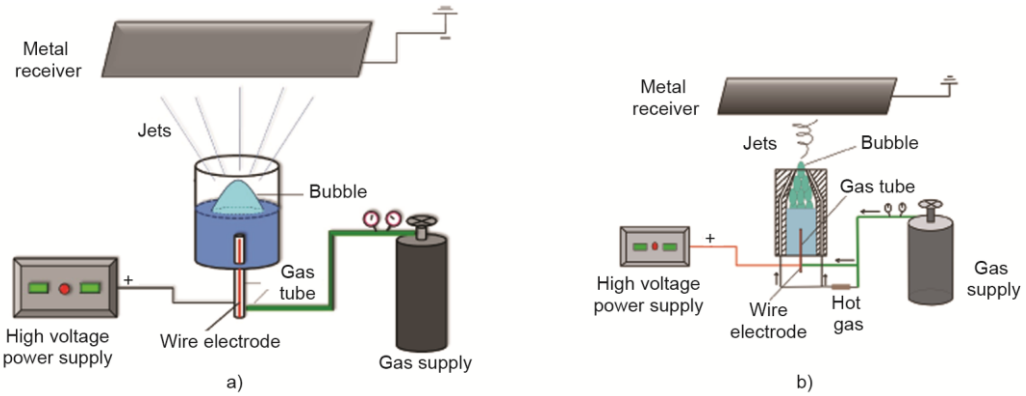


**Figure 1. The experimental set-up of the bubble electrospinning; (a) bubble electrospinning, (b) blown bubble spinning**

## Morphology properties

Rupture process of a bubble under an electrostatic field is illustrated in fig. 2. A ruptured bubble can produce multiple jets as shown in fig. 3. Various morphologies are observed, including continuous nanofibers (fig. 4), thin strips (fig. 5), micro-spheres (fig. 6) and discontinuous backbone-like wrinkled structure (fig. 7).

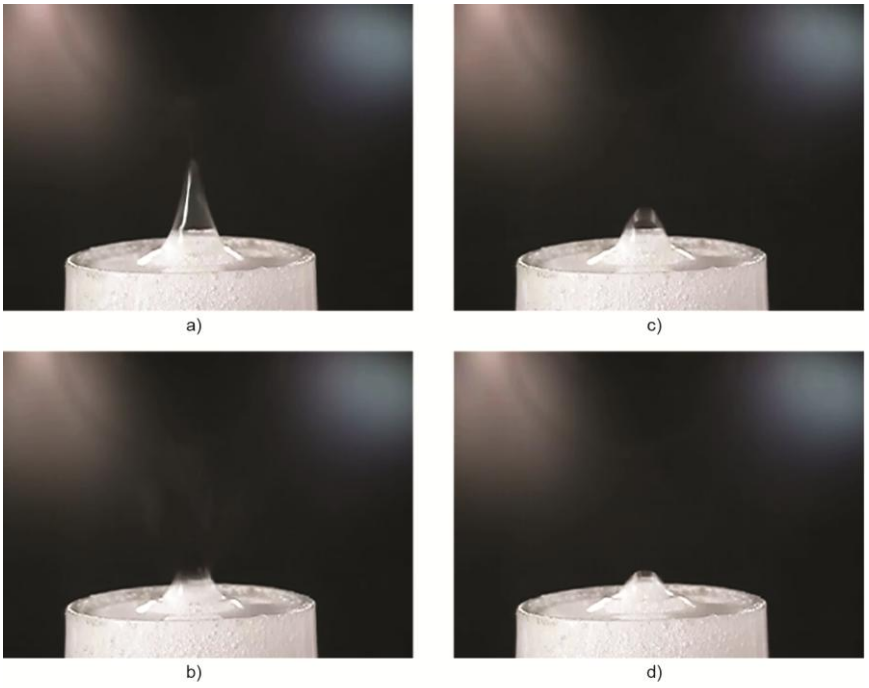


**Figure 2. Rupture process of a bubble under an electrostatic field; (a) the thinning polymer bubble, (b) the bubble is broken somewhere on the top half, the small segments are ejected upwards to the receiver, (c) and (d) the bottom half retracts to form a daughter bubble**

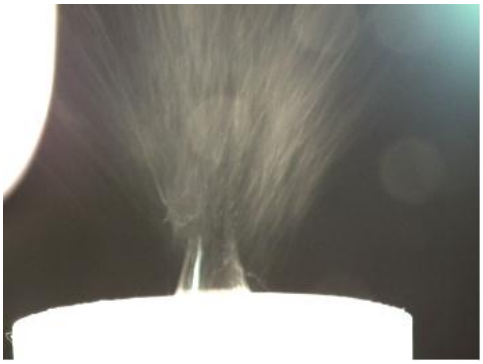

**Figure 3. Multiple charged jets from daughter bubble cascades. The multiple jets come from the previous broken bubble, the bubble we see is a new production of the gas supplier**

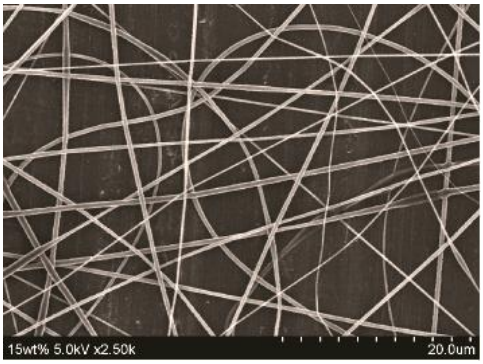


**Figure 4. Continuous nanofibers ranging from 89 nm to 1,012 nm. A 15 wt.% PLA/DMF solution with molecular weight $M_\eta \approx 100000$ is used. The applied voltage is 15 kV and the received distance is 15 cm**

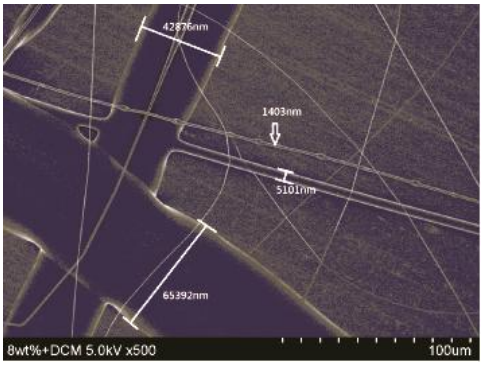


**Figure 5. Stable strips. The concentration of PLA ($M_\eta \approx 100000$) solution with DCM as solvent is 8 wt.%. The applied voltage is 15 kV and the received distance is 15 cm. The strip width ranges from 5,101 nm to 63,392 nm**

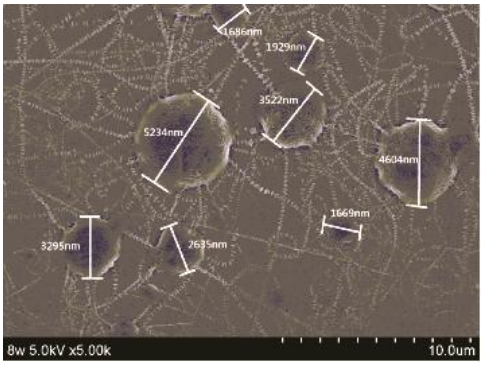


**Figure 6. Micro-spheres ranging from 1,669 nm to 5,234 nm. The spinning solution used here is 8 wt.% Polylactide (PLA) with molecular weight of $M_\eta \approx 100000$, dimethylfomamide (DMF) is used as a solvent. The applied voltage is 15 kV and the distance between the solution surface and the metal receiver is 15cm**

*Critical width of a ruptured film for micro-spheres*

When a bubble is broken, the minimization of surface energy and action of the electronic field result in three distinct morphologies: spheres, fibers, and strips, depending on the size and thickness of the ruptured film.

Consider a strip of a ruptured film as illustrated in fig. 8, we assume the width of the strip is $a$. When the ruptured film area scales with square of the film thickness, it will be retracted into a charged particle, which is ejected and received as a sphere-like particle.

Assume a small piece of ruptured film with area $A$ (see fig. 9) is ejected to the receiver, where it is received as a micro-sphere with radius of $r$.

The mass conversation requires:

$$\frac{4}{3}\pi r^3 = Ah \tag{2}$$

where $h$ is the thickness of the film.

We also assume that the surface of the sphere is approximately equal to that of the ruptured film, that is:

$$A = 4\pi r^2 \tag{3}$$

From eqs. (2) and (3), we can immediately obtain:

$$h = \frac{r}{3} = \frac{d}{6} \text{ for spheres} \tag{4}$$

To form a microsphere, from eqs. (3) and (4), the minimal area of the ruptured film should be:

$$4\pi r^2 = 4\pi(3h)^2 = 36\pi h^2 \tag{5}$$

Generally a square of a ruptured film with $10.6h \times 10.6h$ can be obtained as a sphere with diameter of $6h$ (fig. 6).

The critical width for a sphere, above which fibers or strips can be obtained, can be approximately expressed as:

$$a = 10.6h \tag{6}$$

In case $A < 36\pi h^2$ or $a < 10.6h$, an irregular particle is predicted, see *A* in fig. 7.

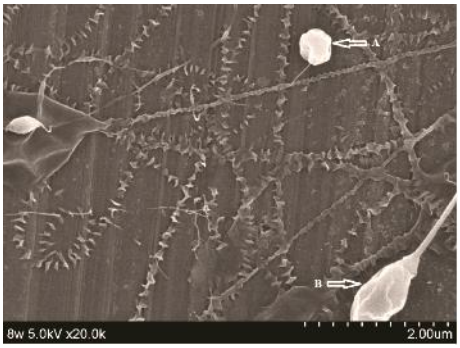


**Figure 7. Discontinuous backbone-like wrinkled materials. The spinning condition is same with that for fig. 3. The average width is 154.33 nm, the average pitch is 141.4 nm. A is an irregular particle, B is a spindle-like structure**

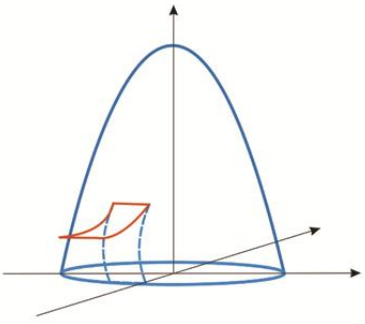

**Figure 8. A strip of a ruptured film resulting from the bursting bubble**

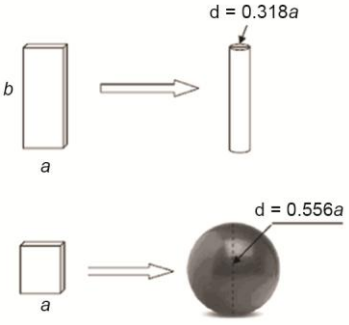


**Figure 9. A ruptured film is retracted as a sphere/cylindrical fiber due to surface tension**

*Critical width of a ruptured film for cylindrical fibers*

When $A > 36\pi h^2$ or $a > 10.6h$, the film might be retracted as a daughter bubble or pulled as a cylindrical fiber or a strip.

Assume a strip with width of $a$ is retracted as a cylindrical fiber (see fig. 9). Similar to the above derivation, we have:

$$\pi r^2 = ah \tag{7}$$

and

$$a = 2\pi r \tag{8}$$

From eqs. (7) and (8), we have:

$$h = \frac{r}{2} = \frac{d}{4} \text{ for fibers} \tag{9}$$

The critical width for a cylindrical fiber can be approximately expressed as:

$$a = 4\pi r \tag{10}$$

*Stable plate-like strip*

In case $a > 4\pi h$, long and thin strip is predicted (see fig. 5). The maximal fiber in fig. 5 is 1,403 nm in diameter, using eq. (9), the maximal thickness of the bubble wall is estimated as 350.75 nm. The smallest trip is 5,101 nm in width (see fig. 5), and we have: $a/h = 5101/350.75 = 14.5 > 4\pi$, satisfying the condition for a strip.

*Natural frequency of thin plate and discontinuous backbone-like wrinkled materials*

In case $10.6h < a < 4\pi h$, an irregular structure is obtained. When $a > 4\pi h$, a thin plate-like strip is formed, which is received on the metal receiver as a strip (fig. 5). The strips are, however, instable, when they are disturbed, they pulsate (that is, they oscillate in size) at their natural frequency, and its configuration corresponds to its nature frequency, fig.10.

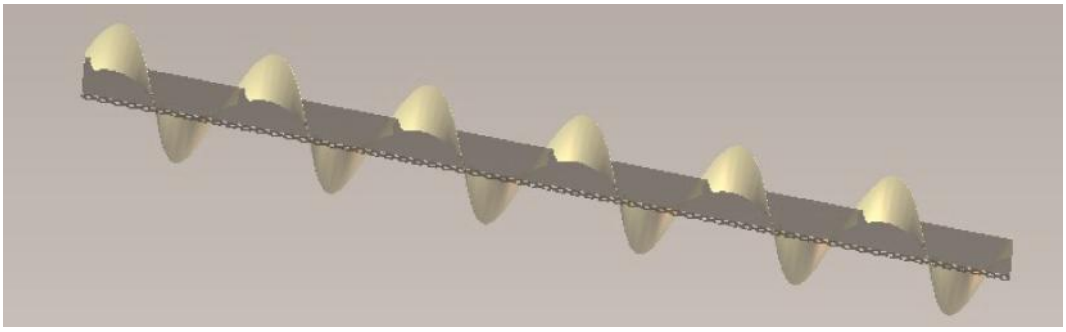

**Figure 10. Mode shape of the thin plate corresponding to its natural frequency**

Consider a rectangular plate with thickness of $h$, width of $a$, and lengthy of $b$, the governing differential equation for the thin plate is:

$$\frac{\partial^4 w}{\partial x^4} + 2\frac{\partial^4 w}{\partial x^2 \partial y^2} + \frac{\partial^4 w}{\partial y^4} = \frac{\rho g \omega^2}{D} w \tag{11}$$

where $w(x, y)$ is the transverse displacement of the midsurface of the plate, $E$ – elastic modulus, $\nu$ – Poisson's ratio, $\omega$ – natural frequency, and $D = (Eh^3)/[12(1-\nu^2)]$ the flexural rigidity.

The variational principle for eq. (11) can be written as [23, 24]:

$$J(w) = \iint_A \left[ \frac{1}{2}\left(\frac{\partial^2 w}{\partial x^2}\right)^2 + \frac{1}{2}\left(\frac{\partial^2 w}{\partial y^2}\right)^2 + \left(\frac{\partial^2 w}{\partial x^2}\right)\left(\frac{\partial^2 w}{\partial y^2}\right) - \frac{1}{2}\frac{\rho h\omega^2}{D} w^2 \right] \mathrm{d}A \tag{12}$$

The total strain energy $V$ of the plate is:

$$V = \frac{D}{2}\iint_A \left\{ \left(\frac{\partial^2 w}{\partial x^2}\right)^2 + \left(\frac{\partial^2 w}{\partial y^2}\right)^2 + 2\left(\frac{\partial^2 w}{\partial x^2}\right)\left(\frac{\partial^2 w}{\partial x^2}\right) \right\} \mathrm{d}A =$$

$$= \frac{D}{2}\int_0^a \int_0^b \left\{ \left(\frac{\partial^2 w}{\partial x^2}\right)^2 + \left(\frac{\partial^2 w}{\partial y^2}\right)^2 + 2\left(\frac{\partial^2 w}{\partial x^2}\right)\left(\frac{\partial^2 w}{\partial x^2}\right) \right\} \mathrm{d}x\,\mathrm{d}y \tag{13}$$

The total kinetic energy $T$ of the plate bending is:

$$T = \frac{\rho h\omega^2}{2}\iint_A w^2 \mathrm{d}A = \frac{\rho h\omega^2}{2}\int_0^a \int_0^b w^2 \mathrm{d}x\,\mathrm{d}y \tag{14}$$

We assume fixed-free-free-free boundary conditions, and use the following trial function:

$$w(x, y) = A\left(1 - \cos\frac{\pi x}{2a}\right) \tag{15}$$

where $A$ is a constant.

Using the Rayleigh method, we can estimate the natural frequency as [23, 24]:

$$\omega^2 \le \frac{V}{T} \tag{16}$$

Combining the above relations, we obtain:

$$\omega \le \frac{0.583}{a^2}\sqrt{\frac{D}{\rho h}} \tag{17}$$

or

$$\omega \le \frac{0.583}{a^2}\sqrt{\frac{Eh^3}{12(1-\nu^2)\rho h}} = \frac{0.583h}{a^2}\sqrt{\frac{E}{12(1-\nu^2)\rho}} \tag{18}$$

We, therefore, obtain the following criterion for strips:

$$\omega = \frac{kh}{a^2} \tag{19}$$

where $k = 0.583\ \{E/[12\ (1 - \nu^2)\rho]\}^{1/2}$ is a constant depending upon the modulus and density.

The mode shape and the natural frequency are given in fig. 7, which is verified by the experimental result given in fig. 7, where the average width of the strip is about 154.33 nm, and $\lambda/4 = 141.4$ nm, where $\lambda$ is the wavelength corresponding to the natural frequency $\omega = v/\lambda$, where $v$ is the phase speed. We re-write eq. (19) in the form:

$$a = \beta\sqrt{h\lambda} \tag{20}$$

where $\beta = (k/v)^{1/2}$, which can be determined experimentally. Using the criterion for a strip, $a > 4\pi h$, we have $\beta = (4\pi a/\lambda)^{1/2} = 1.85$.

Various morphologies are summarized in tab. 1.

**Table 1. Morphologies of the various obtained materials by the bubble electrospinning**

| Conditions | Morphologies |
|---|---|
| $a < 10.6h$ | Irregular particles, see A in fig. 7 |
| $a = 10.6h$ | Spheres with diameter of 6*h*, see fig. 6 |
| $10.6h < a < 4\pi h$ | Irregular structure between sphere and fiber, spindle-like (see B in fig. 7), diamond-like and ellipsoid structure |
| $a = 4\pi h$ | Cylindrical fibers with diameter of 4*h*, see fig. 4 |
| $a > 4\pi h$ and $a \neq \alpha\sqrt{h\lambda}$ | Stable strips, see fig. 5 |
| $a = \alpha\sqrt{h\lambda}$ | Discontinuous backbone-like wrinkled materials, see fig. 7 |
| $a \neq 4\pi h$ | Daughter bubbles |

### *A criterion for bead formation*

The force balance of the charged jet gives [9, 10]:

$$\frac{\mathrm{d}}{\mathrm{d}z}\left(\frac{u^2}{2}\right) = \frac{2\sigma E}{\rho r} + \frac{1}{\rho}\frac{\mathrm{d}\tau}{\mathrm{d}z} \tag{21}$$

where $u$ is the velocity, $\rho$ – the liquid density, $\sigma$ – the surface charge, $r$ – the radius of the jet, $E$ – the applied electric field, and $\tau$ – the viscous force.

Conservation of mass gives [9, 10]:

$$\pi r^2 \rho u = Q \tag{22}$$

where $Q$ is the flow rate, $r$ – the radius of the jet, and $u$ – the velocity.

Conservation of charges gives [9, 10]:

$$2\pi r\sigma u + k\pi r^2 E = I \tag{23}$$

where $k$ is the dimensionless conductivity of the fluid.

The current in the charged jet is mainly composed of two parts: the bulk conduction current and surface convection current.

*Newtonian flow*

As the electrospinning process is extremely complex, an exact solution is almost impossible, and an approximate one outlining the main properties is very much needed.

In the electrospinning, we assume that the total current and flow rate keep unchanged; $I$ in eq. (23) and $Q$ in eq. (22) are constants. Using the Chauchy's inequality:

$$ab \le \frac{1}{4}(a+b)^2, \quad a>0, \quad b>0 \tag{25}$$

we can simplify eq. (21) in an inequality form [26]:

$$\frac{\mathrm{d}}{\mathrm{d}z}\left(\frac{u^2}{2}\right) = \frac{2\pi r\sigma u \cdot k\pi r^2 E}{\pi^2 \rho k r^2 u} + \frac{1}{\rho}\frac{\mathrm{d}\tau}{\mathrm{d}z} \le \frac{(2\pi r\sigma u \cdot k\pi r^2 E)^2}{4\pi^2 \rho k r^4 u} + \frac{1}{\rho}\frac{\mathrm{d}\tau}{\mathrm{d}z} = \frac{I^2}{4\pi k Q r^2} + \frac{1}{\rho}\frac{\mathrm{d}\tau}{\mathrm{d}z} \tag{26}$$

Considering $I$ and $Q$ are constants in eq. (26), we re-write the force balance equation in the following approximate form:

$$\frac{\mathrm{d}}{\mathrm{d}z}\left(\frac{1}{2}u^2\right) = \frac{I^2}{4\pi k Q r^2} + \frac{1}{\rho}\frac{\mathrm{d}\tau}{\mathrm{d}z} \tag{27}$$

This equation holds when:

$$2\pi r\sigma u = k\pi r^2 E \tag{28}$$

If a Newtonian flow is considered, $\tau = \mu\partial u/\partial z$ , eq. (28) reduces to a non-linear differential equation in the form:

$$\frac{\mathrm{d}}{\mathrm{d}z}\left(\frac{1}{2}u^2\right) = \frac{I^2}{4\pi k Q r^2} + \frac{\mu}{\rho}\frac{\mathrm{d}^2 u}{\mathrm{d}z^2} \tag{29}$$

Using eq. (22), we have:

$$\frac{1}{2}\left(\frac{Q}{\pi\rho}\right)^2 \frac{\mathrm{d}}{\mathrm{d}z}(r^{-4}) - \frac{I^2}{4\pi k Q r^2} - \frac{\mu Q}{\pi\rho^2}\frac{\mathrm{d}}{\mathrm{d}z}\left(\frac{\mathrm{d}}{\mathrm{d}z}r^{-2}\right) = 0 \tag{30}$$

This equation can be solved by the variational iteration method, the homotopy perturbation method, or others [27].

In eq. (20), the left term is the inertia force, the middle term the electronic force acting on the charged jet, and the last term is the viscous force. At the initial stage, the electronic force is dominant, and eq. (30) can be further simplified as:

$$\frac{1}{2}\left(\frac{Q}{\pi\rho}\right)^2 \frac{\mathrm{d}}{\mathrm{d}z}(r^{-4}) = \frac{I^2}{4\pi k Q r^2} \tag{31}$$

This equation is approximately valid for the stable jet.

Solving eq. (31), we have:

$$r = \frac{1}{2\sqrt{\frac{\pi\rho^2 I^2}{2kQ^3}z + \frac{1}{4r_0^2}}} \tag{32}$$

where $r_0$ is the initial radius of the jet when $z = 0$. This relationship is experimentally verified in [28].

When the jet reaches the critical point where the acceleration becomes zero, instability of the jet occurs. In the instability stage, we assume that the acceleration is zero. Accordingly eq. (30) reduces to:

$$\frac{I^2}{4\pi kQr^2} + \frac{\mu Q}{\pi\rho^2}\frac{\mathrm{d}^2}{\mathrm{d}z^2}(r^{-2}) = 0 \tag{33}$$

or

$$\frac{\mathrm{d}^2}{\mathrm{d}z^2}(r^{-2}) + \frac{I^2\rho^2}{4\pi kQ^2}r^{-2} = 0 \tag{34}$$

Solving eq. (34) yields:

$$r^{-2} = A\cos(\omega z + \theta_0) \tag{35}$$

where $A$ and $\theta_0$ can be determined by the conditions at the critical point, and $\omega$ is the frequency defined as:

$$\omega = \frac{I\rho}{2Q\sqrt{k\mu}} \tag{36}$$

Equation (35) hints that the jet radius oscillates in the instability process. Due to surface tension, necking of the radius results in beads, which are periodically distributed when received on the metal receiver as illustrated in fig. 11.

In case $\omega \to 0$, beadless fibers can be obtained. In order to obtain smooth nanofibers without beads, according to eq. (36) the following issues can be effectively considered:

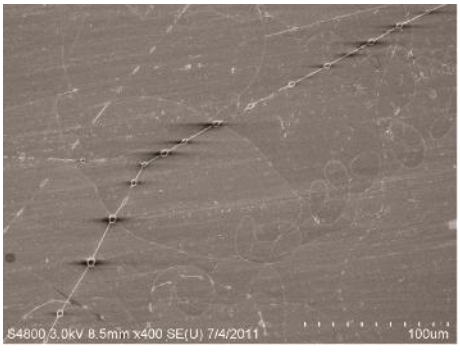


**Figure 11. Beads in electrospun fibers by bubble electrospinning**

*– Increase of k in eq. (23)*

This can be achieved by adding salt additives in the solution or by increasing the conductivity of the solution, see experiment in [15].

*– Increase of viscosity of the solution*

Decrease of solvent in the solution can reduce beads, oppositely, if the solvent (*e. g*. water) concentration increases, the viscosity of the electrospun solution will decrease greatly. As a result, beads are predicted as observed in [29]; and when it reaches a threshold, the necking tension due to the oscillation of the jet size makes the jet broken, only separately drops are obtained [29].

Additionally the flow rate, applied voltage, and solution density will also affect the bead distribution, see discussion in [29].

*Non-Newtonian flow*

The viscous force in eq. (21) for non-Newtonian flow can be expressed in the form

$$\tau = \mu\frac{\partial u}{\partial z} + \varepsilon\left(\frac{\partial u}{\partial z}\right)^n \tag{37}$$

where $\mu$ is the viscosity coefficient, and $\varepsilon$ and $n$ are constants.

Using the mass conservation equation, eq. (22), and the charge conservation equation, eq. (23), we can simplify eq. (37):

$$\frac{\mathrm{d}}{\mathrm{d}z}\left(\frac{u^2}{2}\right) = \frac{E(I - k\pi r^2 E)}{\pi r^2 u\rho} + \frac{1}{\rho}\frac{\mathrm{d}}{\mathrm{d}z}\left[\mu\frac{\partial u}{\partial z} + \alpha\left(\frac{\partial u}{\partial z}\right)^n\right] \tag{38}$$

or

$$\frac{\mathrm{d}}{\mathrm{d}z}\left(\frac{u^2}{2}\right) = \frac{E(I - k\pi r^2 E)}{Q} + \frac{1}{\rho}\frac{\mathrm{d}}{\mathrm{d}z}\left[\mu\frac{\partial u}{\partial z} + \alpha\left(\frac{\partial u}{\partial z}\right)^n\right] \tag{39}$$

Replacing $u$ in eq. (39) by $Q/(\pi^2\rho)$, we obtain:

$$\frac{1}{2}\left(\frac{Q}{\pi\rho}\right)^2\frac{\mathrm{d}}{\mathrm{d}z}(r^{-4}) = \frac{E(I - k\pi r^2 E)}{Q} + \frac{1}{\rho}\left\{\frac{\mathrm{d}}{\mathrm{d}z}\frac{\mu Q}{\pi\rho}\frac{\mathrm{d}}{\mathrm{d}z}(r^{-2}) + \alpha\left(\frac{Q}{\pi\rho}\right)^n\left[\frac{\mathrm{d}}{\mathrm{d}z}(r^{-2})\right]^n\right\} \tag{40}$$

We introduce a new function, $U$, defined as:

$$U = r^{-2} = \frac{\pi\rho u}{Q} \tag{41}$$

Equation (40) becomes:

$$\left(\frac{Q}{\pi\rho}\right)^2 U\frac{\mathrm{d}U}{\mathrm{d}z} = \frac{E(I - k\pi U^{-1}E)}{Q} + \frac{\mu Q}{\pi\rho^2}\frac{\mathrm{d}^2U}{\mathrm{d}z^2} + \frac{1}{\rho}\alpha\left(\frac{Q}{\pi\rho}\right)^n\frac{\mathrm{d}}{\mathrm{d}z}\left(\frac{\mathrm{d}U}{\mathrm{d}z}\right)^n \tag{42}$$

Re-arranging eq. (22), we obtain the following non-linear differential equation:

$$U'' + a - \frac{b}{U} - cUU' + d(U')^{n-1}U'' = 0, \quad U(0) = U_0, \quad U'(0) = \tau_0 \tag{43}$$

where $a = \dfrac{\pi\rho^2 EI}{\mu Q^2}$, $b = \dfrac{k\pi^2\rho^2 E^2}{\mu Q^2}$, $c = \dfrac{Q}{\mu\pi}$, and $d = \dfrac{\alpha n}{\mu}\left(\dfrac{Q}{\pi\rho}\right)^{n-1}$.

The non-linear differential equation, eq. (43), is difficult to be solved exactly, and an approximate solution is much needed to outline the basic property of the solution. This paper gives a simple analytical approach to eq. (43) with physical understandings.

When a jet is ejected from a Taylor cone, it will be accelerated until to a threshold value $u_\infty$, and oscillation of jet size and jet velocity occurs afterwards. Accordingly the solution of eq. (43) is assumed to be have the form:

$$U = U_\infty(1 - \mathrm{e}^{-\beta z}) + U_0 \cos \omega z \tag{44}$$

where $U_\infty$, $\beta$, and $\omega$ are unknown to be further determined by some a residual method, *e. g*., the least square method.

A criterion for oscillatory jet diameter is urgently important for the morphology of the obtained fibers. We assume that the critical point locates at $z = z_c$, after which the jet diameter oscillates. When $z \geq z_c$, eq. (24) can be approximated as:

$$U = U_\infty + U_0 \cos \omega z \tag{45}$$

Substituting eq. (25) into eq. (23) results in the residual:

$$R(z) = U'' + a - \frac{b}{U} - cUU' + d(U')^{n-1}U'' \tag{46}$$

Setting $R(z_c) = 0$, we obtain:

$$-U_0\omega^2 + a - \frac{b}{U_\infty + U_0} = 0 \tag{47}$$

or

$$\omega = \sqrt{\frac{a}{U_0} - \frac{b}{U_0(U_\infty + U_0)}} = \sqrt{\frac{\pi\rho^2 EI}{\mu Q^2 U_0} - \frac{k\pi^2\rho^2 E^2}{\mu Q^2 U_0(U_\infty + U_0)}} = \frac{\rho}{Q}\sqrt{\frac{\pi E}{\mu U_0}\left(I - \frac{k\pi E}{U_\infty + U_0}\right)} \tag{48}$$

A criterion for the oscillatory jet diameter requires $\omega > 0$, that is:

$$I > \frac{k\pi E}{U_\infty + U_0} \tag{49}$$

The oscillatory jet size will finally lead to periodic beads on obtained fibers. Equation (48) has some same properties as eq. (36), salt additives, solvents, flow rate, applied voltage, and solution density will affect the bead distribution. Additionally, according to eq. (48), the initial and ultimate jet velocities will also affect the bead distribution, while the non-Newtonian property is not the main factor for bead morphology. To verify our prediction, an experiment was carried out, the SEM illustration with beads is given in fig. 12. The space between two adjacent beads has an inverse relationship with frequency, that is:

$$T \propto \frac{1}{\omega} \tag{50}$$

Assuming that the fiber diameter is *d* between two adjacent beads, according to the mass conservation equation, eq. (22), we have:

$$U_\infty = \frac{4Q}{\pi d^2 \rho} \tag{51}$$

We also assume that $U_\infty$ □ $U_0$, using the relationships, eqs. (48) and (50), we obtain:

$$T = \frac{p}{\sqrt{1 - qd^2}} \tag{52}$$

where $p$ and $q$ are constants.

Using the data in fig. 12, the average space between adjacent beads can be expressed in the form:

$$T = \frac{2675.6}{\sqrt{1 - 0.00006d^2}} \tag{53}$$

where the units of $T$ and $d$ are in nanometers. Figure 13 compares the theoretical prediction of eq. (53) with experimental data, showing relatively good agreement.

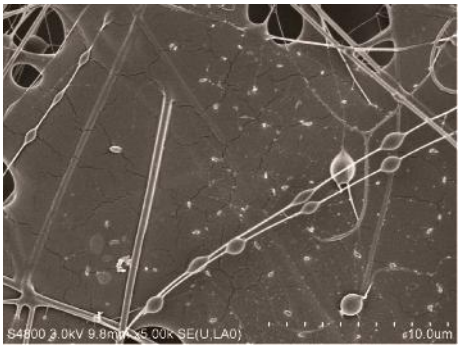


**Figure 12. Electrospun nanofibers with beads**

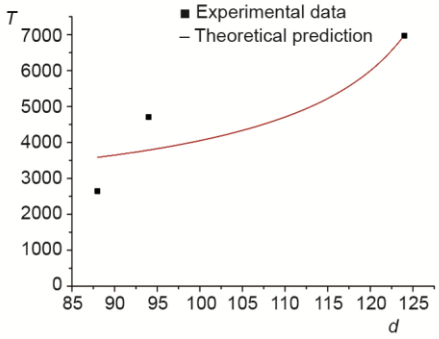


**Figure 13. Experimental data and theoretical prediction**

According to eq. (58), the initial jet velocity will also greatly affect the morphology of the obtained fibers. In classical electrospinning, the initial velocity depends mainly upon the surface tension of the solution and the applied voltage, in the bubble electrospinning, it depends mainly upon the surface tension of the polymer bubble and applied voltage. While the surface tension of the bubble can be adjusted by bubble size, temperature, and air pressure inside and outside of the bubble [6].

### *Nanoporous materials*

In electrospinning process, when the voltage surpasses a threshold value, electrostatic forces overcome the surface tension and a fine charged jet is ejected which is accelerated by a constant external electric field and the jet will become thinner and thinner until it reaches a threshold value. At the same time the density of polarized charges on the surface becomes higher and higher and the distance between charges become smaller and smaller. As a result the Coulomb force might become big enough to dilate the jet to cause nanoporous structure on the surface. In order to verify the prediction, we prepare a triple liquor system. The desired porous structure could be obtained by varying the applied voltage.

Poly butylenes succinate-co-bytylene terephthalate (PBST) with a molecular weight of 20,000 g/mol was supplied by Shanghai Institute of Organic Chemistry. PBST pellets were dissolved in a mixed solvent of iso-propylalcohol and chloroform with a weight ratio 9:1. The

solvents were bought from Shanghai Chemical Reagent Co., Ltd.. All materials were used without any further purification. PBST pellets were dissolved in the mixed solvent with the weight ratio 1:9.

The electrospinning set-up includes a high voltage power supply (up to 50 kV), a syringe, a syringe pump, a flat metal needle and a grounded collector. The collective distance was 12 cm, surrounding temperature was 25 ºC and relative humidity was 60%. In the electrospinning process, a charged polymer solution is extruded toward a grounded collector plate. At sufficiently high electric field, the charged polymer stream is whipped around, leading to the formation of a non-woven mat. The diameter of the orifice is 0.7 mm, the voltage is adjusted to 20-33 kV and the flow rate is adjusted artificially.

The morphology of the electrospun non-woven mats was investigated by a Scanning Electron Microscope (SEM). The films were collected on an SEM disk and coated with gold before photographing. SEM micrographs are illustrated in figs. 14-17.

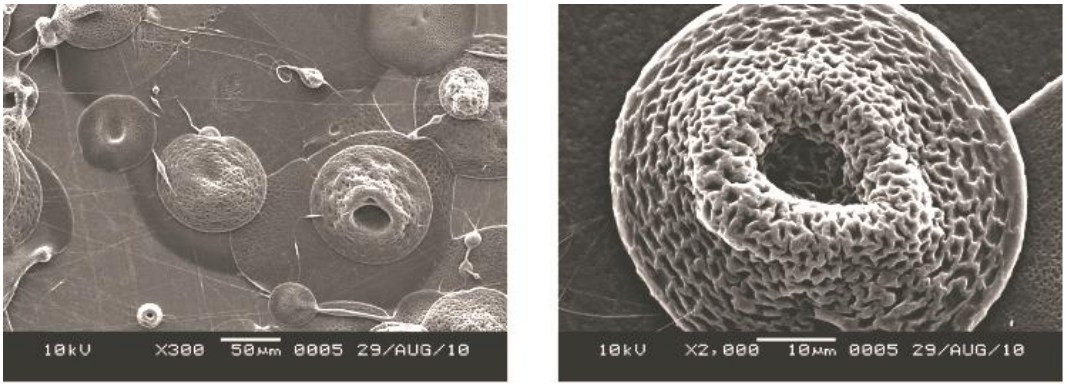


**Figure 14. SEM images of the porous PBST electrospun mat with the voltage supplied 20 kV**

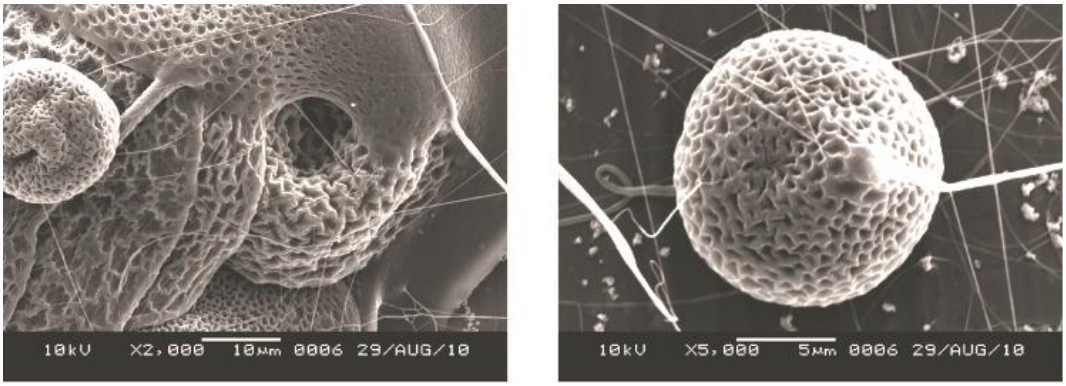


**Figure 15. SEM images of the porous PBST electrospun mat with the voltage supplied 25 kV**

During the electrospinning process, the charged jet is accelerated by a constant external electric field and the spinning velocity probably reached maximum and perhaps exceeded the velocity of sound in air in a very short time before the spinning became unstable.

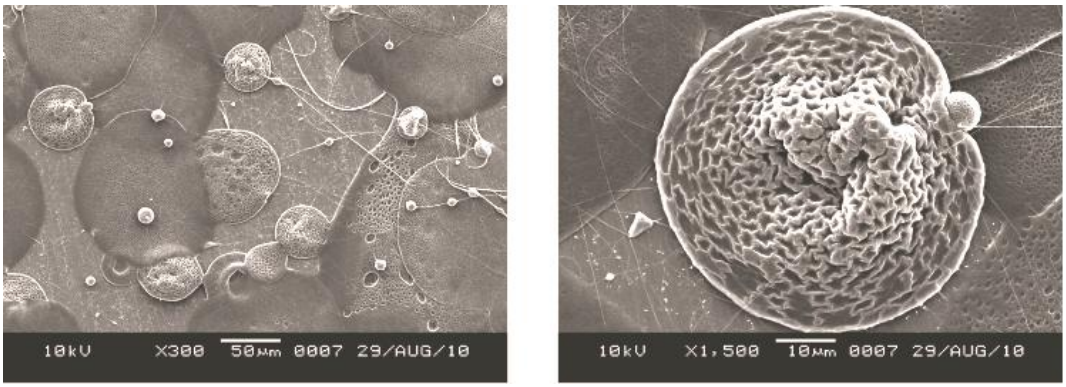


**Figure 16. SEM images of the porous PBST electrospun mat with the voltage supplied 30 kV**

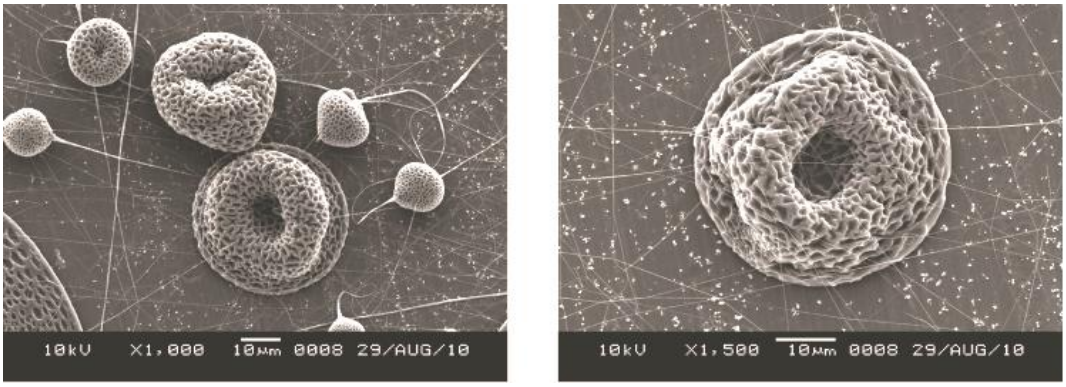


**Figure 17. SEM images of the porous PBST electrospun mat with the voltage supplied 33 kV**

According to the mass conservation equation $\pi r^2 \rho u = Q$, the radius of the jet decreases with the increase of the velocity of the incompressible charged jet. Surface charges are compacted together tighter and tighter during the electrospinning process as illustrated in fig. 18. There must exist a critical minimal radius $r_{cr}$ for the charged jet $r \le r_c$ for continuous ultrafine fibers and the critical maximal velocity is:

$$u_{cr} = Q/\pi\rho r_{cr}^2 \tag{54}$$

However, the velocity can exceed this critical value $u_{cr}$ if a higher voltage is applied.

When $u > u_{cr}$, there is a trend to compact the surface charges and the Coulomb force overcomes the surface tension of the charged jet. As a result the jet is dilated suddenly to cause nanoporous structure on the surface. The Coulomb force of two charges is:

$$F_q = k\frac{q_1 q_2}{d^2} \tag{55}$$

where $d$ is the distance between two charges, $q_1$ and $q_2$ are the electrical quantity of the two adjacent charged particles and $qF_d$ is the Coulomb force.

When the applied voltage surpasses a threshold value for fabrication of continuous nanofibers, higher voltage has a stronger tendency to compact the surface charges more close-

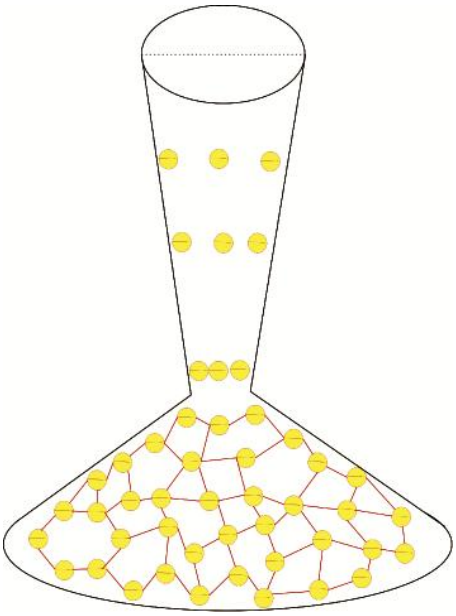

**Figure 18. Detachment of a charged nanojet (The surface charges are compacted during the electrospinning)**

ly and a higher Coulomb force is predicted. Detachment or break off of the nanojet results in a larger hat-like nanoporosity.

This is a general strategy for the synthesis of nanoporous materials by electrospinning, the porous sizes having uniform but tunable diameters can be controlled by the voltage applied. The flexibility and adaptation provided by the method make our methodology a strong candidate for producing nanoporous materials.

## Conclusions

The mathematical analysis based on natural laws is carried out, and morphology of the obtained fibers is elucidated theoretically. Our results are necessary to understanding nanoscience, which bridges between the deterministic classic mechanics and the indeterministic quantum mechanics [25]. Generally nanomaterials can remarkably enhance the mechanical properties, remarkably improve surface energy and surface reactivity, and have excellent thermal and electric conductivity, independent of their bulk materials. Because of ultra improvement of the high specific surface, the new discontinuous backbone-like materials are potentially of great technological interest for the development of electronic, catalytic, and hydrogen-storage systems, invisibility device (*e. g.* stealth plane), photonic structures, sensors, medicine, pharmacy and drug deliver, and others, The periodic wrinkled structure also enables applications in adsorption, separation, filtering, catalysis, fluid storage and transport, electrode materials or as reactors. Far-reaching implications are emerging for applications including radiation protection, medical implants, cell supports, materials that can be used as instructive 3-D environments for tissue regeneration and others.

## Acknowledgments

The work is supported by PAPD (A Project Funded by the Priority Academic Program Development of Jiangsu Higher Education Institutions), National Natural Science Foundation of China under Grant No.10972053.

## References

[1] Chen, Z. Y., *et al.*, Augmentation of Transgenic Expression by Ultrasound Mediated Liposome Microbubble Destruction, *Mol. Med. Rep*., *5* (2012), 4, pp. 964-970

[2] Akimov, V. V., Dmitriev, E. A., Trushin, A. M., Mass Transfer in the Chemosorption of CO(2) in a Membrane Microbubble Apparatus, *Theor. Found. Chem. Eng.*, *45* (2011), 6, pp. 811-817

[3] Steiner, E., Gastl, M., Becker, T., Protein Changes During Malting and Brewing with Focus on Haze and Foam Formation: a review, *Eur. Food Res. Technol*., *232* (2011), 2, pp. 191-204

[4] Gibbs, J. G., Zhao, Y. P., Autonomously Motile Catalytic Nanomotors by Bubble Propulsion, *Appl. Phys. Lett.*, *94* (2009), 16, 163104

[5] Bird, J. C., *et al.*, Daughter Bubble Cascades Produced by Folding of Ruptured Thin Films, *Nature*, *465* (2010),7299, pp. 759-762
[6] He, J.-H., Effect of Temperature on Surface Tension of a Bubble and Hierarchical Ruptured Bubbles for Nanofiber Fabrication, *Thermal Science*, *16* (2012), 1, pp. 327-330
[7] He, J. *et al.*, BioMimic Fabrication of Electrospun Nanofibers with High-Throughput, *Chaos, Solitons and Fractals*, *37* (2008), pp. 643-651
[8] Liu, Y., *et al.*, The Principle of Bubble Electrospinning and its Experimental Verification, *J. Polym. Eng.*, *28* (2008), 1-2, pp. 55-65
[9] He, J.-H., Liu, Y., Xu, L., Apparatus For Preparing Electrospun Nanofibers: A Comparative Review, *Mater. Sci. Tech.*, *26* (2010), 11, pp. 1275-1287
[10] He, J. *et al.*, *Elelectrospun Nanofibers and their Applications*, Smithers Rapra Update, Shawbury, UK, 2008
[11] Yang, R. R., *et al.*, Bubble-Electrospinning for Fabrication of Nanofibers with Diameter of about 20 nm, *Int. J. Nonlin. Sci. Num.*, *11* (2010), S, pp.163-164
[12] Schwarz, H. A., *Göttingen. Nachr.*, (1884), pp. 1-13
[13] Suzuki, K., *et al.*, Enhancement of Heat Transfer in Subcooled Flow Boiling with Microbubble Emission, *Exp. Therm. Fluid Sci.*, *29* (2005), 7, pp. 827-832
[14] van den Bos, A., *et al.*, Infrared Imaging and Acoustic Sizing of a Bubble Inside a Micro-Electro-Mechanical System Piezo Ink Channel, *J. Appl. Phys. 110* (2011), 3, 034503
[15] Karshafian, R., Burns, P. N., Qi, X. L., Microbubble Destruction-Reperfusion in the Non-Invasive Measurement of the Vascular Targeting Effects of the Anti-Cancer Drug ZD6126, in: *Ultrasonics Symposium* (Eds. D. E. Yuhas, S. C. Schneider), 2002, pp. 1989-1992
[16] Sumetsky, M., Dulashko, Y., Windeler, R. S., Optical Microbubble Resonator, *Optics Lett.*, *35* (2010), 7, pp. 898-900
[17] Zhong, S., *et al.*, Enhanced Homing of Mesenchymal Stem Cells to the Ischemic Myocardium by Ultrasound-Targeted Microbubble Destruction, *Ultrasonics*, *52* (2012), 2, pp. 281-286
[18] de Gennes, P. G., Brochard-Wyart, F., Quere, D., Capillary and Wetting Phenomena: Drops, Bubbles, Pearls, Waves, Springer, 2002
[19] Hilton, J. E., van der Net, A., Dynamics of Charged Hemispherical Soap Bubbles, *EPL*, *86* (2009), 2, 24003
[20] Nejad, H. R., Ghassemi, M., Langroudi, S. M. M., A Molecular Dynamics Study of Nanobubble Surface Tension, *Mol. Simulat.*, *37* (2011), 1, pp. 23-30
[21] Matsumoto, M.,Tanaka, K., Nano Bubble-Size Dependence of Surface Tension and Inside Pressure, *Fluid Dyn. Res.*, *40* (2008), 7-8, pp. 546-553
[22] Tarkan, H. M., Gelinas, S., Finch, J. A., Measurement of Thickness and Composition of a Solvent Film on a Bubble, *J. Colloid Interf. Sci.*, *297* (2006), 2, pp. 732-737
[23] Weaver, W., Timoshenko, S. P., Young, D. H., *Vibration Problems in Engineering*, Wiley-Interscience, New York, USA, 1990
[24] Wei, G. W., Zhao, Y. B., Xiang, Y., The Determination of Natural Frequencies of Rectangular Plates with Mixed Boundary Conditions by Discrete Singular Convolution, *Int. J. Mech. Sci.*, *43* (2001), 8, pp. 1731-1746
[25] El Naschie, M. S., Nanotechnology for the Developing World, *Chaos Soliton. Fract.*, *30* (2006), 4, pp. 769-773
[26] He, J.-H., Wu, Y., Zuo, W. W., Critical Length of Straight Jet in Electrospinning, *Polymer*, *46* (2005), 26, pp. 12637-12640
[27] He, J.-H., An Elementary Introduction to Recently Developed Asymptotic Methods and Nanomechanics in Textile Engineering, *Int. J. Mod. Phys. B*, *22* (2008), 21, pp. 3487-3578
[28] Qin, X.-H., *et al.*, Effect of LiCl on Electrospinning of PAN Polymer Solution: Theoretical Analysis and Experimental Verification, *Polymer*, *45* (2004), 18, pp. 6409-6413
[29] Liu, Y., *et al.*, Controlling Numbers and Sizes of Beads in Electrospun Nanofibers, *Polymer International*, *57* (2008), 4, pp. 632-636

Paper submitted: May 4, 2012
Paper revised: September 1, 2012
Paper accepted: September 14, 2012